

Synthesis of WTe₂ thin films and highly-crystalline nanobelts from pre-deposited reactants

*John B. Mc Manus^{1,2}, Cansu Ilhan^{1,2}, Bastien Balsamo^{2,3}, Clive Downing^{1,2}, Conor P. Cullen^{1,2},
Tanja Stimpfel-Lidner⁴, Graeme Cunningham^{1,2}, Lisanne Peters^{1,2}, Lewys Jones^{2,5}, Daragh
Mullarkey⁵, Igor V. Shvets⁵, Georg S. Duesberg^{1,4}, Niall McEvoy^{1,2*}*

¹ School of Chemistry, Trinity College Dublin, Dublin 2, D02 PN40, Ireland

² AMBER Centre, CRANN Institute, Trinity College Dublin, Dublin 2, D02 PN40, Ireland

³ SIGMA Clermont, Université Clermont Auvergne, F-63000 Clermont–Ferrand, France

⁴ Institute of Physics, EIT 2, Faculty of Electrical Engineering and Information Technology,
Universität der Bundeswehr, 85579 Neubiberg, Germany

⁵ School of Physics, Trinity College Dublin, Dublin 2, D02 PN40, Ireland

KEYWORDS: 2D materials; WTe₂; film conversion; electrodeposition; electron microscopy;
nanoelectronics

*Corresponding author: nmcevoy@tcd.ie

ABSTRACT

Tungsten ditelluride is a layered transition metal dichalcogenide (TMD) that has attracted increasing research interest in recent years. WTe_2 has demonstrated large non-saturating magnetoresistance, potential for spintronic applications and promise as a type-II Weyl semimetal. The majority of works on WTe_2 have relied on mechanically-exfoliated flakes from chemical vapour transport (CVT) grown crystals for their investigations. While producing high-quality samples, this method is hindered by several disadvantages including long synthesis times, high-temperature anneals and an inherent lack of scalability.

In this work, a synthesis method is demonstrated that allows the production of large-area polycrystalline films of WTe_2 . This is achieved by the reaction of pre-deposited films of W and Te at a relatively low temperature of 550 °C. Sputter X-ray photoelectron spectroscopy reveals the rapid but self-limiting nature of the oxidation of these WTe_2 films in ambient conditions. The WTe_2 films are composed of areas of micrometre sized nanobelts that can be isolated and offer potential as an alternative to CVT-grown samples. These nanobelts are highly crystalline with low defect densities indicated by TEM and show promising initial electrical results.

1. INTRODUCTION

Transition metal dichalcogenides (TMDs) are a family of layered materials whose nanoscale forms have been extensively studied over the last number of years. This interest is due to their varied and layer-dependent properties, which gives them a wide range of potential applications.(1, 2)

Unlike some of the more commonly-studied TMDs, such as MoS_2 and WS_2 that exist predominantly in the trigonal prismatic 2H phase, WTe_2 is most stable in the distorted octahedral

T_d phase, making it unique among the Group VI TMDs.(3, 4) This structure means WTe₂ is semimetallic and opens up unique electronic properties, such as topological electronic states.(5) Thorough investigations of the structure and electrical properties of bulk WTe₂ were carried out in the 1950's and 1960's, with particular emphasis placed on its thermoelectric properties.(3, 6-11) However, it is only recently that investigations have focussed on mono- and few-layer forms.

WTe₂ can be considered a layered or 2D material, though it does also have some 1D character due to its distorted octahedral structure. This distortion causes quasi-1D chains of W atoms to be formed within the layers, schematically shown in Fig.1 (a) insert.(4) This leads to a strong anisotropy in properties such as the conductivity and mechanical response within the monolayer.(12) It also manifests in the tendency of WTe₂ crystals to grow anisotropically.(13) The crystals are generally longest along the b crystallographic direction, parallel to the 1D tungsten chains.

Applications-centred studies of WTe₂ have historically focussed on thermoelectrics but more recent studies have examined a much broader range of potentially interesting properties and applications. Experimental investigations of the electronic properties of WTe₂ have demonstrated large, non-saturating magnetoresistance and high charge-carrier mobilities of up to 10,000 cm²V⁻¹s⁻¹.(14-16) There have also been reports of ferroelectricity(17) and superconductivity(18, 19) in WTe₂. Furthermore, it was the first material to be suggested as a potential type-II Weyl semimetal.(20) Since this prediction, there have been a number of experimental reports that have lent credence to this assertion.(21, 22)

Other works have examined WTe₂ for use in applications such as nanoscale electrical interconnects(23), electrocatalysis(24, 25) and as an anode material for Na-ion batteries.(26) Additionally, WTe₂ has been touted as a promising candidate for large-gap quantum spin Hall

insulators(5, 21, 27) Lastly, through electrochemical investigations the possibility of using WTe₂ as a catalyst for the hydrogen evolution reaction (HER) has been examined.(24, 28-31)

The majority of reports, especially those examining its electronic properties, have focused on mechanically-exfoliated flakes from chemical vapour transport (CVT) grown crystals of WTe₂.(14-16, 32-34) While CVT does produce exceptionally high-quality crystals, it is a time and energy intensive process requiring long anneals at temperatures of up to 1000 °C. The subsequent laborious mechanical exfoliation and transfer process also limits the scalability of any devices made using this method.

There has been some work on the bottom-up growth of nanoscale WTe₂, however large-area, reproducible synthesis remains an open challenge.(35, 36) Table 1 gives an overview of a range of publications that synthesised WTe₂ on the nanoscale. Chemical vapour deposition (CVD) growth of WTe₂ has achieved single-crystal monolayers with lateral dimensions on the order of 10s to 100s of micrometres from Te, WO₃ and WCl₆ precursors.(35-37) Despite requiring high growth temperatures, 650 – 800 °C, CVD growth remains the most promising method for high-quality monolayer synthesis. Nevertheless, there remains significant challenges to overcome before large-area, reproducible, layer controlled growth of WTe₂ is achieved.

Large-area growth of polycrystalline films of WTe₂ has however been achieved, with thicknesses ranging from a few to tens of monolayers.(38-41) These films are generally synthesised by the conversion of a pre-deposited W source on a substrate. This is accomplished by exposure of the W source to Te vapour in a controlled atmosphere at an elevated temperature. These methods offer the advantage of producing large-area films in a scalable manner. The final thickness of the film can also be determined by the thickness of the initially deposited W source. These polycrystalline films have grain sizes ranging from less than 10 nm to ~100 nm. This means

that while promising for a range of applications, these films are not suitable for many electronic applications due to high and variable levels of unintentional doping and high densities of scattering centres.(42)

A number of other works have synthesised WTe_2 on the nanoscale using methods such as solution-based growth or molecular beam epitaxy (MBE).(26, 43, 44)

This discussion shows that while substantial progress has been made in the synthesis of nanoscale WTe_2 , the field is far from mature. The majority of works rely on CVT meaning there is a pressing need for further work on alternative lower temperature synthesis methods, especially those which are scalable.

Table 1: Literature review of published synthesis techniques to produce nanoscale WTe_2 .

Ref.	Method Description	Subsequent processing to obtain 2D form	Material Characteristics	Synthesis T (°C)	Growth Time
(14)	CVT	Mechanical exfoliation(ME)	Single-crystal flakes	750	11 days
(45)	CVT	ME	Single-crystal flakes	800	10 days
(32)	CVT	ME	Single-crystal flakes	900	4 days
(46)	CVT	ME	Single-crystal flakes	1000	8 days
(22)	CVT	ME	Single-crystal flakes	800	11 days
(47)	CVT	ME	Single-crystal flakes	1020	5 days
(48)	CVT	ME	Single-crystal flakes	950	3 days
(33)	CVT	ME	Single-crystal flakes	1100	4 days
(35)	CVD, ammonium tungstate hydrate and KCl promoter	None	Monolayer flakes ~350 μm	800	20 min
(37)	CVD, WCl_6/WO_3 precursor	None	Monolayer flakes ~350 μm	820	20 min
(38)	CVD WCl_6 precursor	None	Polycrystalline film; thickness above 5 nm	500	20 min
(36)	CVD, ammonium metatungstate precursor	None	Monolayer flakes ~50 μm	650	6 min
(49)	CVD, WO_3 precursor and KI growth promoter	None	Monolayer flakes 10s μm ,	700	1 hour
(39)	Film conversion, predeposited W/ WO_3	None	Large-area polycrystalline film, thickness 6 nm, grain size ~6 nm	650	60 min
(50)	Film conversion, predeposited WO_3 nanowires	None	Nanowires	500	10 min
(51)	Film conversion, predeposited W, close proximity Ni_xTe_y source	None	Large-area polycrystalline films, thickness - few layer to bulk, 10s nm grain size	500	10-30 min

(40)	Film conversion, predeposited W, need H ₂ present during reaction	None	Large-area polycrystalline film, thickness 1 + nm, grain size 10s nm	800	50 min
(41)	Film conversion, predeposited W and Cu	None/ Mechanical transfer	Large-area polycrystalline film of WTe ₂ nanobelts	500	10 min
(44)	MBE, HOPG/MoS ₂ substrates	None	Large-area films	275	1.5nm hr ⁻¹
(52)	CVT	Sonication	Quantum dots		
(53)	Pulsed laser deposition	None	Polycrystalline film; thickness 5+ nm		
(54)	Pulsed laser deposition	Post-deposition anneal with Te	Highly crystalline, thickness ~100 nm	700	1 nm min ⁻¹ 48hr anneal
(25)	Solution-phase growth		Nanostars		
(55)	Solution-phase growth		Nanostructures, ~200 nm	260	
(43)	Solution-phase film formation, WCl ₄ precursor	Microwave heating	Large-area polycrystalline film, few-layer thickness, grain size 6 nm		

In this work we present a method to synthesise polycrystalline films consisting of WTe₂ nanobelts, with individual nanobelts of up to 10 μm in length. These are synthesised by annealing pre-deposited films of W and Te at a relatively low temperature of 550 °C. Characterisation of the films reveals that their surface is prone to oxidation but this is self-limiting and does not extend into the bulk. Due to their large lateral size, these micrometre-scale, single-crystal nanobelts of WTe₂ can be isolated and characterised individually. The high crystallinity of the nanobelts implies their suitability for applications previously demonstrated using CVT-grown flakes. To show this, individual nanobelts were electrically characterised. The ability to access both large-area films and single-crystalline flakes demonstrates the versatility of this method to produce high-quality samples of WTe₂ in an efficient manner.

2. RESULTS AND DISCUSSION

2.1 Synthesis of WTe₂ films

Films of WTe₂ were synthesised by depositing a layer of W onto a target substrate using Ar-ion sputtering, followed by the electrodeposition of Te on top of this, as shown in Fig. 1(a). The thickness and pattern of the W layer was defined during the sputtering process, while the electrodeposition allowed the Te to be deposited in a controlled and directed manner onto each sample. This method gave local, well-defined quantities of both reactants directly on the sample. This avoided the need for a remote Te source and the challenges associated with this, such as requiring high excess of reactant to be used.

The layers of W and Te were then placed inside nested crucibles and then loaded into a quartz furnace, where they were heated to form WTe₂, shown in Fig. S1(a) The conversion typically took place at a dwell temperature of 550 °C for a period of 90 minutes under an inert atmosphere.

All samples are named based on their starting W thickness, as measured by the deposition tool's quartz crystal monitor (QCM). The sample substrates were SiO₂/Si wafer with a ~300 nm layer of pyrolytic carbon (PyC) to improve the uniformity of the Te film deposition.⁽⁵⁶⁾ The samples studied were ~1 x 1 cm in area but the process could be scaled up to produce larger area samples.

This synthesis method allowed the growth of large-area polycrystalline films of WTe₂. Fig. 1(a)-(c) shows scanning electron microscopy (SEM) images of a typical WTe₂ film synthesised from an initial 20 nm W layer. It is immediately apparent that the surface of the film consists of two differing morphologies. There are discrete patches, with dimensions of up to tens of micrometres, containing elongated WTe₂ nanobelts. The nanobelts are several micrometres in length and have widths of tens to hundreds of nanometres. Surrounding the patches of nanobelts are areas of smaller grains with lengths below 500 nm. The growth of elongated nanobelts is due to the quasi-1D nature

of WTe_2 , similar growth of elongated WTe_2 flakes that has been seen in CVD growth of WTe_2 in a number of works.(26, 35, 57) The 1D chains of W in the lattice would be expected to be parallel to the long axis of the nanobelts.

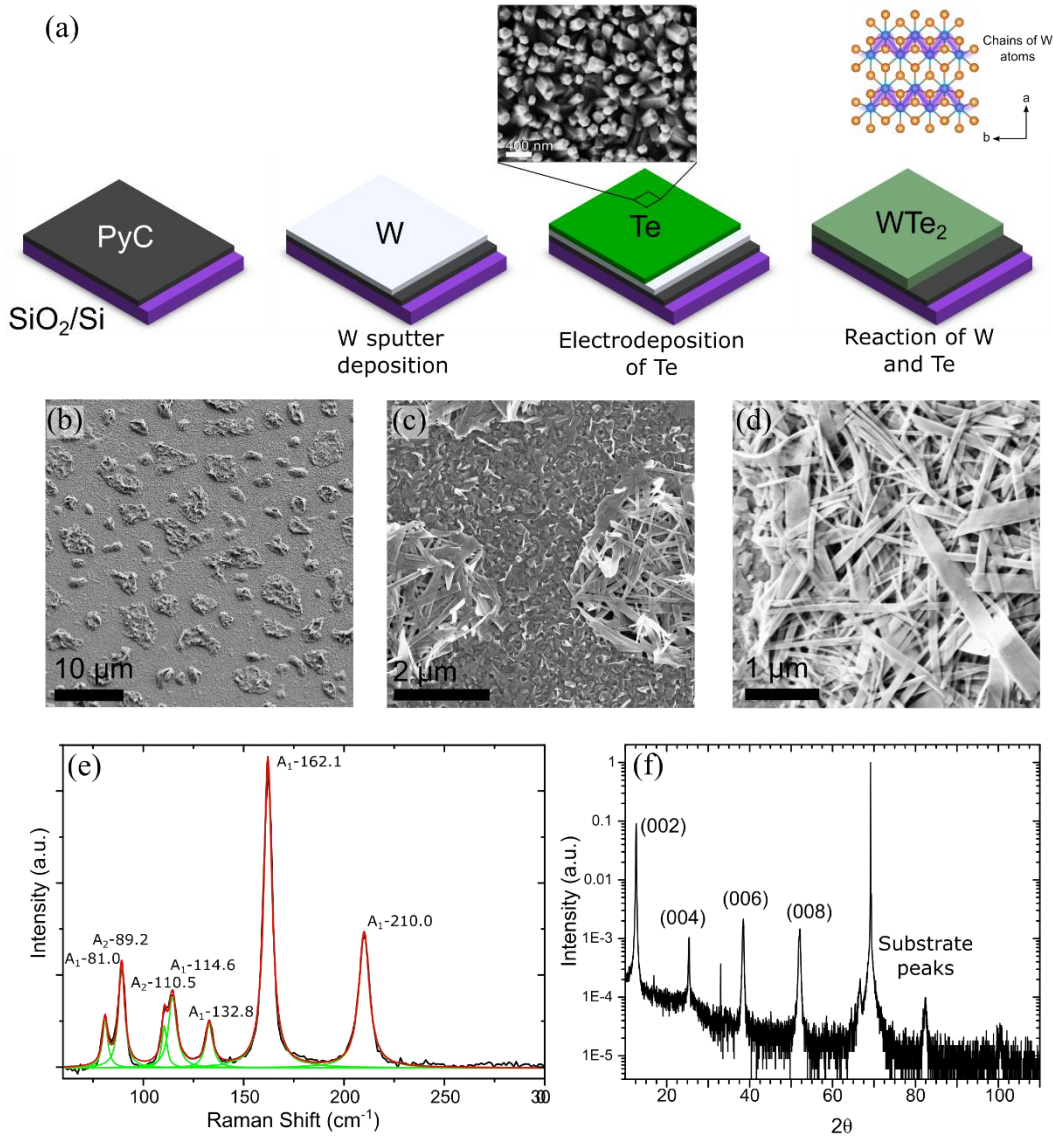


Fig.1 (a) The process steps involved in WTe_2 film synthesis with an SEM image of the surface of the TE film before conversion to WTe_2 . Insert: Diagram of the 1D W atom chains in the WTe_2 structure. (b)-(d) SEM images of the surface of WTe_2 film synthesised from 20 nm initial W layer. (d) Raman spectrum of the same film showing the expected modes of bulk-like WTe_2 . Modes are fitted with Lorentzian peaks to extract positions. (e) XRD diffraction pattern of WTe_2 film showing the (002) and associated reflections. A number of substrate peaks are also visible above 60 degrees.

The WTe₂ films are synthesised in a straight-forward, scalable manner with full coverage over the entirety of the sample. This compares favourably with the majority of previously-reported growth methods for WTe₂ which are by-in-large laborious, time consuming and not scalable. Furthermore, the properties of the films – thickness, grain size – can be tailored by changing the parameters of the initial W and Te depositions.

Compared to typical film conversion methods, which have grain sizes of 10s of nanometres, this work allows the growth of films made up of much larger crystals, on the order of micrometres. This is likely due to the growth occurring at a solid-liquid interface, rather than the typical solid-vapour one. Having the liquid Te in direct contact with the W layer counteracts the low activity of Te and facilitates the synthesis of WTe₂ at the comparatively low synthesis temperature and short time, similar to other works using Ni_xTe_y alloys.(51) Furthermore, H₂ is not required to enable the growth in this work, unlike previously reported methods.(40)

The morphology of these WTe₂ films is also influenced by the material properties - MoTe₂ and PtTe₂ previously grown using this method were found to have significantly different morphologies, with neither showing films consisting of large nanobelts.(56, 58)

Raman analysis, shown in Fig 1(d), provides confirmation of the formation of WTe₂. This spectrum closely matches previously published spectra of bulk-like WTe₂, indicating the successful growth of T_d phase WTe₂ using this method.(59-61) The peaks at 81.0 cm⁻¹, 89.2 cm⁻¹, 114.6 cm⁻¹, 132.8 cm⁻¹, 162.1 cm⁻¹ and 210.0 cm⁻¹ are assigned the symmetry A₁, while the peak at 110.5 cm⁻¹ is A₂.(32, 62) The Raman spectrum does not indicate any modes associated with oxides or other contaminants in the films.

Confirmation of the presence of WTe₂ throughout the surface, was provided by Raman spectroscopy mapping, Fig. S2. While there are two morphologies present on the surface, which

look quite different under optical microscopy and SEM, Raman spectroscopy mapping confirms that they are both T_d WTe_2 .

X-ray diffraction (XRD) further confirmed the conversion of the W and Te films to WTe_2 . XRD results are shown in Fig. 1(e), the diffraction pattern measured is consistent with previously-reported XRD of WTe_2 with the (002), (004), (006) and (008) peaks being most prominent.(3) As the film is polycrystalline, there is a significant background and noise in the diffraction pattern. This made further analysis, such as extracting average grain size, infeasible.

To obtain more quantitative and stoichiometric information, the films were analysed using X-ray photoelectron spectroscopy (XPS). This also gave information on the stability of the films, which can be considered important as previous reports have indicated a strong tendency for WTe_2 to oxidise in ambient conditions. (36, 48, 63)

The XPS results are shown in Fig. 2. Shown in (a) is the W 4f core-level region of WTe_2 , the W 5p and Te 4d core levels are also visible in this energy window however the analysis here will only focus on the W 4f core levels, as these are the most intense. There are two doublets present for the W 4f core level, one associated with WTe_2 and the other with WO_3 . Of the W atoms, 30% are in the form of WO_3 , with the remaining 70% in WTe_2 . Similarly in Fig.2 (b), there are two doublets associated with the Te 3d core level, one corresponding to Te bound to W as WTe_2 and the other for Te in the form of oxides. The Te on the surface is predominantly in the form of WTe_2 , with only 8% of the atoms bound to oxygen. The stoichiometry of the WTe_2 on the surface was found to be $WTe_{1.8}$, indicating a slight deficiency in Te. Finally, the asymmetric nature of the WTe_2 peaks indicates the (semi-)metallic nature of the sample.

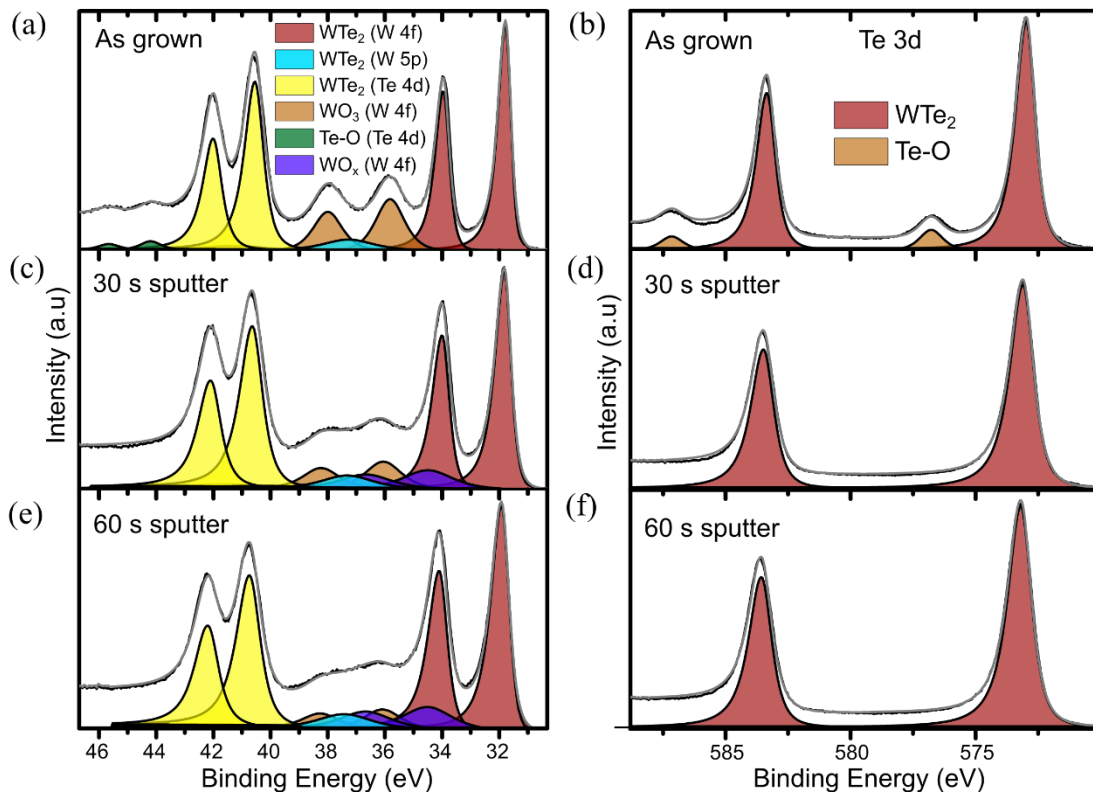


Fig.2 (a), (c), (e) XPS spectra of the W 4f region for a WTe₂ sample as grown, after 30 s of sputtering and after 60 s of sputtering respectively. (b), (d), (f) The same data for the Te 3d binding energy region of the WTe₂ sample

2.2 Oxidation of WTe₂ films

The level of oxidation observed on the surface of the WTe₂ film implies that it is prone to degradation in atmosphere, more so than other telluride TMDs such as MoTe₂ and PtTe₂ that have shown lower oxidation levels when similarly analysed.(56, 58) Previous works on the susceptibility of WTe₂ to oxidation have concluded that the oxidation of the first few atomic layers of WTe₂ is extremely rapid, however the oxidation is self-limiting and tends not to extend far into the bulk. (36, 48, 63) It is this surface layer (less than 10 nm) that is exclusively probed by XPS, potentially leading to an over estimation of the over-all oxidation level of the sample. To offer further understanding of this, the sample was analysed using sputter XPS.

Sputter XPS involves repeated cycles of in-situ sputtering and XPS analysis, allowing the elemental composition at both the surface and at various depths in the bulk of the sample to be measured. The sputter XPS process is described in more detail in the methods section.

Two rounds of 30 seconds Ar sputtering were carried out, with the results shown in Fig. 2(c) – (f). The Te 3d core-level spectra show that after 30 seconds of sputtering only a single doublet corresponding to Te in the form of WTe_2 is visible. The signal of Te bound to oxygen is below the detection limit of the tool, indicating that the Te oxide is only present on the surface with virtually none in the bulk of the sample.

The signal from WO_3 reduces significantly after sputtering, from about 30% initially, to 10% after 60 seconds. During the same time, the percentage of W atoms in the form of WTe_2 remains roughly constant at 70%. The difference is accounted for by the development of a WO_x signal that accounts for slightly less than 20% of W atoms after 60 seconds of sputtering. This WO_x peak is not present in the surface scan but develops after sputtering. All the W peaks broaden after sputtering, due to damage or amorphization caused by the sputtering process.

The sputtering XPS shows that TeO_2 and WO_3 are primarily present on the surface of the films. However, a WO_x signal is present after sputtering, and the percentage of W atoms present as either WO_3 or WO_x is roughly constant throughout. Furthermore, the overall ratio of W to Te on the surface changes after sputtering, with the sample becoming increasingly deficient in Te. The proposed explanation of these observations is that the Te is being preferentially sputtered, meaning that the sample becomes more W rich during this process, and the WO_3 is not being effectively sputtered but rather becoming a substoichiometric WO_x .⁽⁶⁴⁾ This also correlates with previous reports that indicate the self-limiting nature of WTe_2 oxidation. Furthermore, this conclusion also

aligns with why no strong oxide signal is observed in the Raman spectroscopy – Raman is much less surface-sensitive than XPS so the WTe_2 signal remains dominant.

2.3 WTe_2 growth mechanism

The majority of films in this work were synthesised at a temperature of 550 °C, however WTe_2 was successfully grown over a range of temperatures. Fig. 3(a) shows Raman spectra of films synthesised at a range of temperatures. At 350 °C, the only Raman peaks visible are attributed to elemental Te.⁽⁶⁵⁾ For all growth temperatures between 450 °C and 650 °C characteristic peaks associated with bulk-like WTe_2 are observed. No discernible peaks are visible in the 750 °C scan indicating that no WTe_2 or Te are present following growth at this temperature.

Some understanding of the influence of growth temperature can be achieved by examining the binary phase diagram for W-Te, reproduced in Fig. S3 from reference.⁽⁶⁶⁾ As the sample reaches the Te melting point - 450 °C - a liquid WTe_x alloy forms at the boundary between the W and Te, as a result of the W dissolving into the liquid Te. It is clear from the phase diagram, that in this temperature range (450 °C to 650 °C) the alloy remains liquid for only a very small percentage W, beyond which it becomes supersaturated. This means that, as more W dissolves into the Te, solid WTe_2 crystals begin to nucleate and grow within the liquid alloy. Concurrent with this the Te is evaporating, further driving the growth of WTe_2 crystals. If the growth time is sufficiently long, all unreacted Te will evaporate, leaving a film solely consisting of WTe_2 during the cool-down. Below 450 °C the formation of an intermixed layer is greatly reduced due to the Te not melting, dramatically hindering the growth, as shown by the poor WTe_2 Raman signal at 400 °C and the absence of any discernible WTe_2 Raman signal at 350 °C.

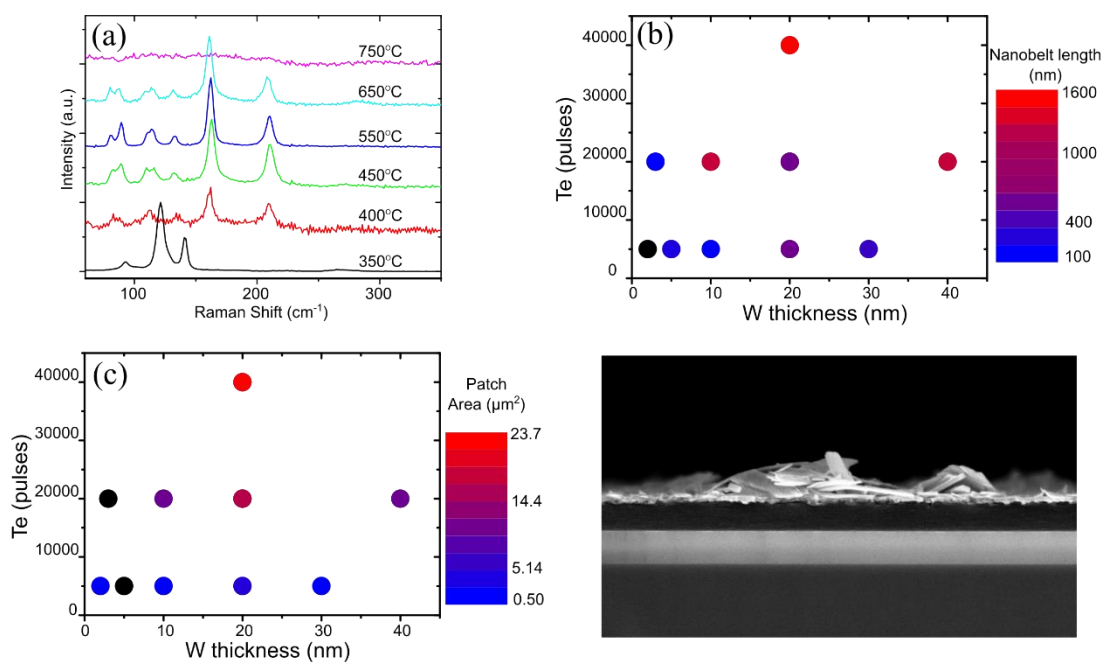


Fig.3 (a), Raman of WTe₂ films synthesised at a range of temperatures between 350 °C and 750 °C. At 350 °C only the signal for Te is present, between 450 °C and 650 °C there is a strong signal corresponding to bulk-like WTe₂. At 400 °C there is a weak WTe₂ signal and at 750 °C there are no discernible Raman peaks. (b) Plot of the variation average nanobelt length (100 nm – 1600 nm) with changes in the amount of W and Te present. The thickness of the initial layer of W was varied between 2 and 40 nm. Between 5,000 and 40,000 pulses of Te were electrodeposited on the surface. Red indicates longer nanobelt patches. (c) Variation of patch area with changes to W and Te amounts. (d) Cross-section SEM image of a cleaved substrate and WTe₂ film showing raised patches of WTe₂ nanobelts.

The upper bound of ~650 °C cannot be understood from the phase diagram, which indicates stability of WTe₂ up to ~1000 °C. The proposed reason for the upper bound seen here is that the Te evaporates too quickly to react effectively, or any WTe₂ that does form decomposes through loss of Te due to the Te-deficient environment.(67, 68) This loss would not occur in CVT growth systems due to the vessel being sealed, maintaining high Te concentrations throughout the growth, allowing the use of higher growth temperatures.

By changing the initial quantity of W and Te on the samples it was possible to control the thickness of the films and also the average sizes of the WTe₂ grains/nanobelts. The average nanobelt size was primarily determined by the quantity of Te present, except for the thinnest films

where both the W and Te quantity were important, as shown in Fig. 3(b). This figure shows W and Te quantities on the x- and y-axes respectively, with the average nanobelt size indicated by the colour of the data points. The lesser effect of W suggests that below a certain point it limits the growth, but above a particular threshold, it no longer has a strong influence on nanobelt size. The average length of the nanobelts could be varied between <100 nm and 1600 nm over the parameter space examined.

The size of the WTe_2 crystals grown in the film is affected by the Te quantity in two ways. Firstly, more Te provides more reactant in general, allowing larger crystal growth. Secondly, since the reaction to form WTe_2 occurs in the liquid Te alloy, more Te provides a greater duration for the reaction to occur before the Te vaporises.

The two distinct morphologies on the surface can be similarly explained. During the growth the Te dewets and forms droplets on the surface. These droplets serve as areas of high local reactant quantity, and long growth times, enabling much larger crystals to grow than in surrounding areas. Furthermore, the area of these patches containing larger WTe_2 nanobelts also increases with increasing Te quantity, as shown in Fig. 3(c).

These results correlate well with previously published reports for a similar system in the work of Kwak *et al.*(41) However a notable difference is that if one looks at a cross-section SEM of the films in this work, shown in Fig. 3(d), it is clear that the droplets were raised above the majority of the surface and that the WTe_2 crystals grew within them. This suggests that the W tends to dissolve into the Te rather than the Te etching down into the W, as was proposed in the previous work.

2.4 Characterising Individual Nanobelts

The majority of film conversion growth methods result in polycrystalline films with grain sizes between 10 and 100 nm. In contrast, the films produced in this work can be optimised to have nanobelts with lengths of up to 10 μm . The larger crystal size and discrete and separate nature of the nanobelts allowed us to develop a method to isolate individual WTe_2 nanobelts for further study by transferring them onto another substrate. This allowed examination of individual nanobelts in a manner not possible for a film. Details of this transfer method are given in Fig. S4.

Fig. 4(a) and (b) show optical and atomic force microscopy (AFM) images of the nanobelts on the destination substrate. The largest nanobelts measure about 10 μm long, width of ~ 600 nm and thicknesses of ~ 130 nm. While flakes with smaller lateral sizes were correspondingly thinner (10 – 20 nm), all nanobelts examined are nevertheless well into the range of displaying bulk-like characteristics.

The transfer of individual WTe_2 nanobelts made it possible to examine them using transmission electron microscopy (TEM). Initial analysis of the nanobelts was carried out using high-resolution TEM (HRTEM). Fig. 4(c) is a HRTEM image of a nanobelt, with the corresponding fast Fourier transform (FFT) shown in the insert. These highlight the crystalline nature of the WTe_2 with clear lattice fringes visible in the TEM image and discrete spots in the FFT.

To further examine the crystal structure and quality, annular dark-field scanning TEM (ADF-STEM) was carried out on the nanobelts. This analysis allowed atomic-resolution images to be captured, shown in Fig. 4(d). This image clearly shows that these nanobelts have a high level of crystallinity, with no grain boundaries visible over the area examined.

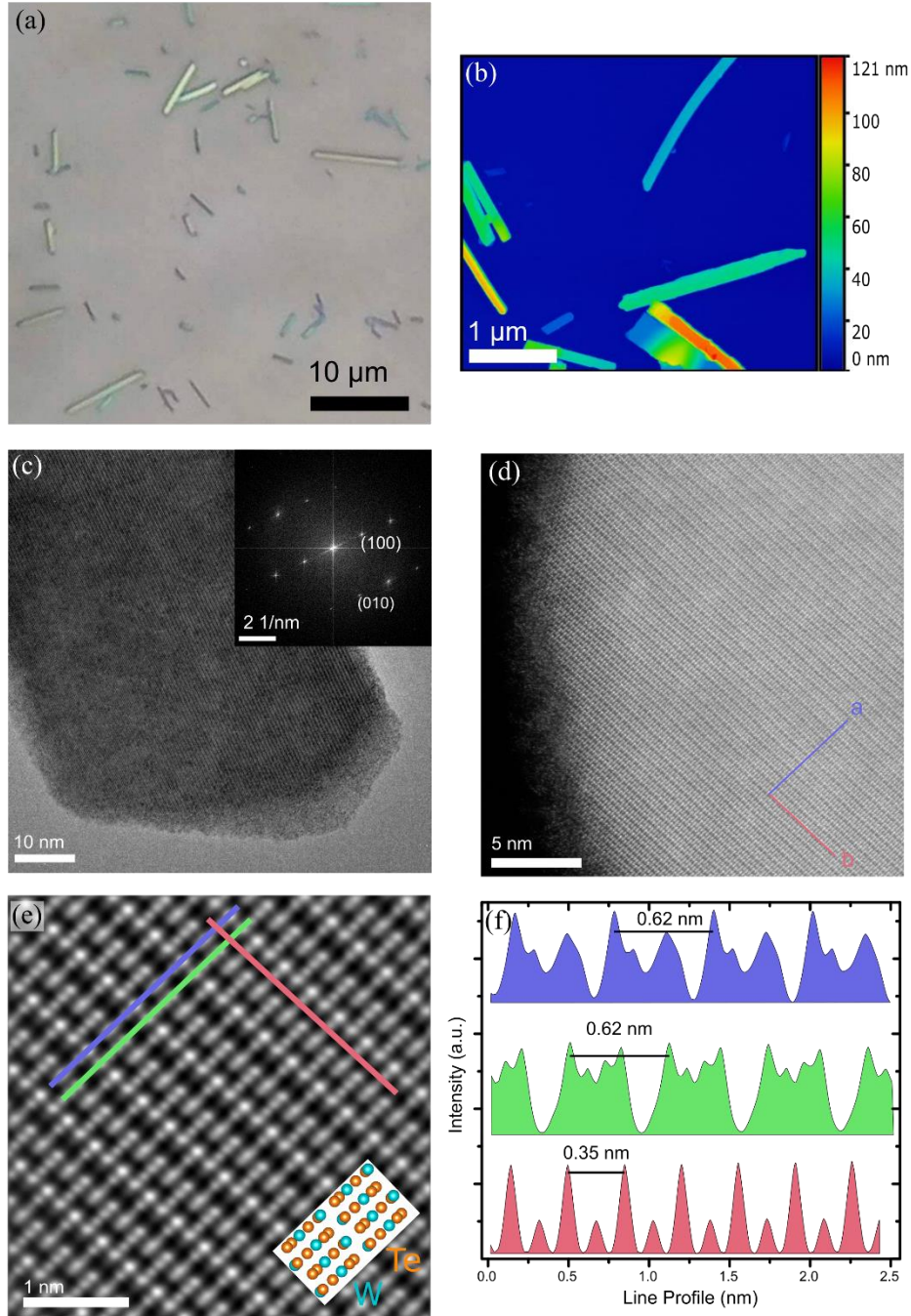


Fig.4 (a) Optical image of transferred WTe_2 nanobelts. (b) AFM image of same sample (c) HRTEM image of a WTe_2 nanobelt, insert FFT of image (c). (d) ADF-STEM image of the edge of a WTe_2 nanobelt, with the WTe_2 crystallographic directions marked. (e) Atomic-resolution ADF image of WTe_2 crystal, compiled by averaging areas of (c). Insert: atomic positions of WTe_2 for appropriate crystallographic direction (f) Profiles of intensity measured from lines indicated in (d)

STEM images were taken from either end of a WTe₂ nanobelt, several micrometres in length, the FFTs of these images are shown in Fig. S5. These match to a very close degree, offering further confirmation of the single-crystalline nature of the nanobelts. It should be noted that there is some distortion in the images shown here. The orthogonal crystalline directions have measured angles of $\sim 87^\circ$ between them. This is thought to be most likely due to small stage drift or slight misalignment of the crystalline axis during imaging.(69)

The STEM analysis indicates the highly-crystalline nature of the nanobelts, without significant defect densities visible. As there are no visible grain boundaries within the nanobelts they are potentially comparable to mechanically-exfoliated flakes from CVT-grown crystals. This could open up a much quicker and lower-temperature synthesis route to produce micrometre size WTe₂ flakes for a range of studies.

By applying a spatial averaging and scan-distortion correction technique to Fig. 4(d), the image shown in Fig. 4(e) was obtained.(70) This averaging technique is discussed further in the methods section.(71) This shows very clear atomic resolution giving the expected T_d structure of WTe₂. This matches well to previously published analysis of WTe₂.(4, 41)

Measuring the intensity along the two crystallographic directions of this image, gave the line profiles shown Fig. 4(f).(72) The red profile shows a repeating pattern every 0.35 nm. This matches closely to the lattice constant of WTe₂ along the [010] crystallographic direction of 0.3496 nm. While the repeat period in the orthogonal direction of 0.62 nm, is very close to the unit cell length of 0.6282 nm for WTe₂ along the [100] direction. Using this information, along with the spacings obtained from the FFTs, allowed the conclusion to be drawn that it is the (001) lattice planes that are being examined in this case. A model of the expected atomic positions in this case is shown in Fig. 4(e) insert. This matches quite well to the alternating lines of atoms observed in the STEM

image. When viewed from this direction, atoms in WTe_2 do not line up in perfect atomic columns meaning that exact atomic positions cannot be assigned despite the clarity of the image.

Examining again Fig. 4(c), it is possible to assign the lattice directions a and b, as shown by the arrows. This confirms that the W zigzag or 1D chains, which form along the b crystallographic direction in T_d WTe_2 , are parallel to the long axes of the nanobelt as expected.

2.5 Electrical characterisation

Electron-beam lithography (EBL) was used to contact individual WTe_2 nanobelts. This allowed the electrical behaviour of the crystalline nanobelts WTe_2 to be probed without the influence of junctions between WTe_2 grains. An AFM map of a device is shown in Fig. 5(a), with corresponding height profile in Fig. 5(b).

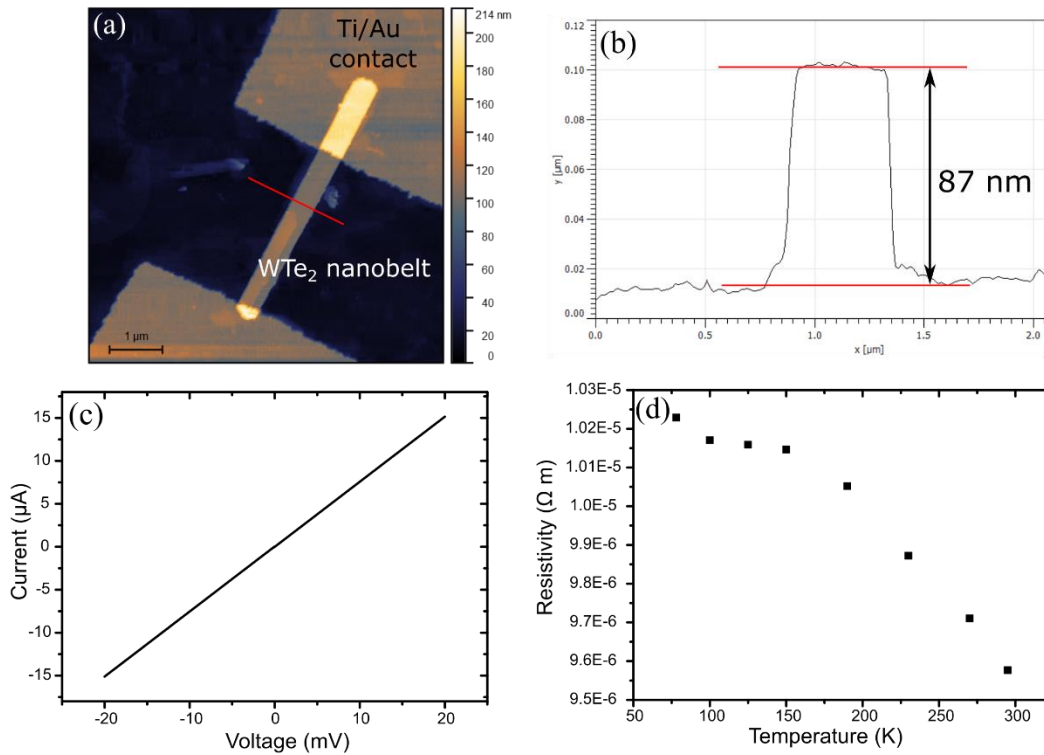


Fig.5 (a) AFM image of the contacted WTe₂ nanobelt device (b) Height profile of the nanobelt along the line marked in (a). Two-terminal IV measurement of the WTe₂ nanobelt device. (d) Plot showing the change in resistivity of the nanobelt as the temperature is increased from 78K to 293K

The two-terminal IV response of a nanobelt device is shown in Fig. 5(c). The device response is Ohmic over the measured region. The dimensions from AFM allowed the resistivity of the device to be calculated, this was found to be $9.3 \times 10^{-6} \Omega\text{m}$. This low resistivity is expected due to the semimetallic nature of WTe₂. Interestingly, this resistivity matches almost exactly the values measured by Song *et al.* in their paper on the potential use of single-crystal WTe₂ nanobelts as electrical interconnects in nanoelectronics.(23) Their synthesis method requires the deposition of films of W and Cu that are then exposed to Te vapour. This causes a CuTe_x alloy to form, in which the WTe₂ grows. Following this a post-growth etch is needed to remove residual CuTe_x.(41) The synthesis method in this work is more straight-forward and does not require a post-growth etch offering a potential advantage. The nanobelts produced here have a very similar form, crystallinity

and electrical response to the work of Song *et al.*, indicating that the WTe₂ is likely of a similar quality and thus suitable for similar applications.

The temperature dependence of the WTe₂ nanobelt resistance was investigated, with the results shown in Fig. 5(d). The nanobelt shows very little change in resistivity with temperature; becoming ~10% less resistive as the temperature is increased from 77K to 300K. A small change in resistivity is unsurprising for a semimetallic material, though a trend of decreasing resistivity with temperature is more usually associated with a semiconductor. There is some variation in literature reports of WTe₂ resistivity change as a function of temperature. Some works on thin crystals of WTe₂ show a reduction in resistivity with increasing temperature due to Anderson localization effects. However that was for much thinner (3 - 4 layer) flakes, while the nanobelt examined here was ~120 layers.(15, 23) Works on thicker samples of WTe₂ generally show increasing resistivity as the temperature is increased. The magnitude of this effect is reported as being between ~5% and ~500% change over a similar temperature window to that examined in this work.(23, 32, 54, 73) It is possible that effects such as the formation of a potential barrier at the contacts due to surface oxidation may also be influencing results seen in this and other works. Further studies would be required to fully understand the observed result.

3. CONCLUSIONS

We developed a method to synthesise large-area films of WTe₂ from pre-deposited W and Te layers. Successful conversion of these layers to WTe₂ films was confirmed with various spectroscopies. SEM showed that the polycrystalline films consisted of two different morphologies, one being regions of nanobelts up to 10 μm in length. The films were found to be stoichiometric WTe₂ but with a significant amount of surface oxidation. In line with previous

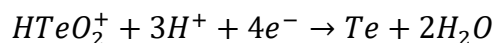
reports of WTe₂ oxidation being self-limiting, the oxide level in the bulk of the film was found to be substantially lower.

Further to this we isolated individual nanobelts from the films to allow additional characterisation. Through TEM analysis the nanobelts were shown to be highly crystalline with low defect densities. Combined with promising initial electrical results, this indicates the potential for these nanobelts to be used in investigations where previously mechanically-exfoliated CVT crystals were used.

This ability to yield both WTe₂ films and nanobelts in a straight-forward manner at relatively low synthesis temperature is a compelling advantage of this growth method over those used in many previous studies.

4. EXPERIMENTAL METHODS

A film of W was deposited onto the substrate using a Gatan PECS Ar-ion sputtering tool. A layer of Te was subsequently deposited on top of this by electrodeposition. Te was reduced from solution, 0.02 M TeO₂ in 1 M nitric acid, in an electrochemical cell. A platinum counter electrode and a Ag/AgCl reference electrode were used. This is shown in Fig. S1(b). The reduction proceeded *via* the reaction(74):



A pulsing sequence was used during the deposition, this consisted of 10 ms pulses of -0.3 V applied to the working electrode with respect to the reference electrode with 50 ms gaps between these. Varying the number of pulses in a deposition served to control the quantity of Te deposited

on the sample. Using a pulsing potential was found to yield a more uniformly deposited film of Te.(74) Further detail is given in a previous work using a similar method to synthesise MoTe₂.(56)

The substrates used throughout the work are PyC on a 300 nm thermal SiO₂ on Si wafer. The PyC layer is not necessary but served to improved conductivity during the electrodeposition. The PyC was grown by CVD of acetylene at 950°C for 30 mins on SiO₂/Si substrates in a hot-wall, quartz-tube furnace.(75)

Following the Te deposition, the films were converted to WTe₂ in an ATV PEO 604 quartz furnace under a nitrogen atmosphere at a pressure of ~700 mbar. The growth temperature was typically 550 °C but other growth temperatures were also investigated. Nested crucibles were used to maintain a high partial pressure of Te in the vicinity of the samples while avoiding contaminating the furnace with high quantities of Te, as shown in Fig. S1(a). The temperature was ramped at 180 °C min⁻¹ and held at the growth temperature for 90 mins. The samples were then allowed to cool to near room temperature (<30 °C) under N₂ over a period of ~3 hours before removal from the furnace. During the cooling, at ~320 °C, the pressure was lowered from ~700 mbar to 13 mbar to ensure removal of any remaining Te. All samples are named by referring to the thickness of the starting W film.

Nanobelts of WTe₂ were mechanically transferred from the growth substrate using adhesive Nitto Denka BT-150E-CM tape. A schematic of this process is shown in Fig. S4. In order to grow the films with the largest possible WTe₂ nanobelts, samples with 40 nm of W and 40,000 pulses of Te were used for transferring nanobelts from.

SEM images were obtained with a Karl Zeiss Supra microscope operating at 3 kV accelerating voltage, 30 µm aperture and a working distance of ~3-4 mm.

The XRD measurement was performed on a Bruker D8 Discover with a monochromated Cu K-alpha source.

A WITec Alpha 300R with a 532 nm excitation laser, with a power of $\sim 200 \mu\text{W}$, was used to collect the Raman spectra shown herein. All Raman measurements were taken using a spectral grating with 1800 lines/mm and a 100x objective lens. Raman spectra shown are averages of maps which were generated by taking scans every 400 nm in the x and y directions, typically over an area of $20 \times 20 \mu\text{m}$, making each spectrum an average of $\sim 2,500$ spectra.

X-ray photoelectron spectroscopy (XPS) spectra were taken with a PHI VersaProbe III instrument equipped with a micro-focused, monochromatic Al K α source (1486.6 eV) and a dual-beam charge neutralization was used. Core level spectra were recorded with a spot size of $100 \mu\text{m}$ and a pass energy of 69 eV using PHI SmartSoft VersaProbe software, and processed with PHI MultiPak 9.8. Sputter XPS depth profiling was conducted using 1 keV Ar ions. Binding energies were referenced to the adventitious carbon signal at 284.8 eV. Spectral components were fitted using a Shirley background subtraction and appropriate line shapes. Relative atomic percentages were calculated using the relative sensitivity factors provided by the software CasaXPS

AFM was carried out on a Bruker Multimode 8 in ScanAsyst Air mode using Nanosensor PointProbe Plus tips.

HRTEM analysis was performed in an FEI Titan TEM at an acceleration voltage of 300 kV. Atomic-resolution STEM images were obtained with a Nion UltraSTEM200, using a HAADF detector, operated at 200 kV.

An overview of how STEM averaging was performed is that initially a small area of the sample ($4 \text{ nm} \times 4 \text{ nm}$ in this case) with atomic resolution is chosen. The software then scans the remainder of the image and finds all the areas with which this image matches to a high degree. All of these

areas (300 in this analysis) are then extracted and stacked to form an average image.(71) Further image processing then removes any distortion in the image.(70)

For electrical measurements samples were patterned by EBL before Ti/Au (5 nm/100 nm) contacts were deposited using electron-beam evaporation.

ACKNOWLEDGEMENTS

J.B. Mc M. acknowledges an Irish Research Council scholarship, Project 204486, Award 13653.

N. M. acknowledges support from SFI through 15/SIRG/3329 and 12/RC/2278_P2. G. S. D.

acknowledges the support of SFI through PI_15/IA/3131. LJ acknowledges SFI and the Royal Society Fellowship URF/RI/191637. The SEM and (S)TEM imaging for this project was carried out at the Advanced Microscopy Laboratory (AML), Trinity College Dublin, Ireland. The AML (www.tcd.ie/crann/aml) is an SFI supported imaging and analysis centre, part of the CRANN Institute and affiliated to the AMBER centre.

ETHICAL STANDARDS

The authors declare that the experiments in this work comply with the current laws of the country in which they were performed.

CONFLICT OF INTEREST

There are no conflicts of interest to declare.

REFERENCES

1. Gong C, Zhang Y, Chen W, Chu J, Lei T, Pu J, et al. Electronic and Optoelectronic Applications Based on 2D Novel Anisotropic Transition Metal Dichalcogenides. *Advanced Science*. 2017;4(12):1700231.
2. Liu Y, Weiss NO, Duan X, Cheng H-C, Huang Y, Duan X. Van der Waals heterostructures and devices. *Nature Reviews Materials*. 2016;1(9):16042.

3. Brown BE. The crystal structures of WTe₂ and high-temperature MoTe₂. *Acta Crystallographica*. 1966;20(2):268-74.
4. Lu N, Zhang C, Lee C-H, Oviedo JP, Nguyen MAT, Peng X, et al. Atomic and Electronic Structures of WTe₂ Probed by High Resolution Electron Microscopy and ab Initio Calculations. *The Journal of Physical Chemistry C*. 2016;120(15):8364-9.
5. Qian X, Liu J, Fu L, Li J. Quantum spin Hall effect in two-dimensional transition metal dichalcogenides. *Science*. 2014;346(6215):1344-7.
6. Revolinsky E, Beerntsen D. Electrical Properties of the MoTe₂-WTe₂ and MoSe₂-WSe₂ Systems. *Journal of Applied Physics*. 1964;35(7):2086-9.
7. Champion JA. Some properties of (Mo, W) (Se, Te)₂. *British Journal of Applied Physics*. 1965;16(7):1035-7.
8. Kabashima S. Electrical Properties of Tungsten-Ditelluride WTe₂. *Journal of the Physical Society of Japan*. 1966;21(5):945-8.
9. Troadec JP, Bideau D, Guyon E. Transport properties of conducting and semiconducting anisotropic mixtures. *Journal of Physics C: Solid State Physics*. 1981;14(32):4807-19.
10. Knop O, Haraldsen H. A NOTE ON THE SYSTEM WOLFRAM-TELLURIUM. *Canadian Journal of Chemistry*. 1956;34(8):1142-5.
11. Goldschmidt VM. Crystal structure and chemical constitution. *Transactions of the Faraday Society*. 1929;25(0):253-83.
12. Torun E, Sahin H, Cahangirov S, Rubio A, Peeters FM. Anisotropic electronic, mechanical, and optical properties of monolayer WTe₂. *Journal of Applied Physics*. 2016;119(7):074307.
13. Kim Y, Jhon YI, Park J, Kim JH, Lee S, Jhon YM. Anomalous Raman scattering and lattice dynamics in mono- and few-layer WTe₂. *Nanoscale*. 2016;8(4):2309-16.
14. Ali MN, Xiong J, Flynn S, Tao J, Gibson QD, Schoop LM, et al. Large, non-saturating magnetoresistance in WTe₂. *Nature*. 2014;514(7521):205-8.
15. Wang L, Gutiérrez-Lezama I, Barreateau C, Ubrig N, Giannini E, Morpurgo AF. Tuning magnetotransport in a compensated semimetal at the atomic scale. *Nature Communications*. 2015;6(1):8892.
16. Wang Y, Wang L, Liu X, Wu H, Wang P, Yan D, et al. Direct Evidence for Charge Compensation-Induced Large Magnetoresistance in Thin WTe₂. *Nano Letters*. 2019;19(6):3969-75.
17. Fei Z, Zhao W, Palomaki TA, Sun B, Miller MK, Zhao Z, et al. Ferroelectric switching of a two-dimensional metal. *Nature*. 2018;560(7718):336-9.
18. Fatemi V, Wu S, Cao Y, Bretheau L, Gibson QD, Watanabe K, et al. Electrically tunable low-density superconductivity in a monolayer topological insulator. *Science*. 2018;362(6417):926-9.
19. Kang D, Zhou Y, Yi W, Yang C, Guo J, Shi Y, et al. Superconductivity emerging from a suppressed large magnetoresistant state in tungsten ditelluride. *Nature Communications*. 2015;6(1):7804.
20. Soluyanov AA, Gresch D, Wang Z, Wu Q, Troyer M, Dai X, et al. Type-II Weyl semimetals. *Nature*. 2015;527(7579):495-8.
21. Li P, Wen Y, He X, Zhang Q, Xia C, Yu Z-M, et al. Evidence for topological type-II Weyl semimetal WTe₂. *Nature Communications*. 2017;8(1):2150.

22. Zhang W, Wu Q, Zhang L, Cheong S-W, Soluyanov AA, Wu W. Quasiparticle interference of surface states in the type-II Weyl semimetal WTe₂. *Physical Review B*. 2017;96(16):165125.
23. Song S, Kim S-Y, Kwak J, Jo Y, Kim JH, Lee JH, et al. Electrically Robust Single-Crystalline WTe₂ Nanobelts for Nanoscale Electrical Interconnects. *Advanced Science*. 2019;6(3):1801370.
24. Li J, Hong M, Sun L, Zhang W, Shu H, Chang H. Enhanced Electrocatalytic Hydrogen Evolution from Large-Scale, Facile-Prepared, Highly Crystalline WTe₂ Nanoribbons with Weyl Semimetallic Phase. *ACS Applied Materials & Interfaces*. 2018;10(1):458-67.
25. Srinivaas M, Wu C-Y, Duh J-G, Hu Y-C, Wu JM. Multi-walled carbon-nanotube-decorated tungsten ditelluride nanostars as anode material for lithium-ion batteries. *Nanotechnology*. 2019;31(3):035406.
26. Hong M, Li J, Zhang W, Liu S, Chang H. Semimetallic 1T' WTe₂ Nanorods as Anode Material for the Sodium Ion Battery. *Energy & Fuels*. 2018;32(5):6371-7.
27. Zhang W, Wu Q, Zhang L, Cheong S-W, Soluyanov AA, Wu W. Quasiparticle interference of surface states in the type-II Weyl semimetal $\{\mathbf{WTe}\}_2$. *Physical Review B*. 2017;96(16):165125.
28. Gholamvand Z, McAteer D, Backes C, McEvoy N, Harvey A, Berner NC, et al. Comparison of liquid exfoliated transition metal dichalcogenides reveals MoSe₂ to be the most effective hydrogen evolution catalyst. *Nanoscale*. 2016;8(10):5737-49.
29. Zhou Y, Silva JL, Woods JM, Pondick JV, Feng Q, Liang Z, et al. Revealing the Contribution of Individual Factors to Hydrogen Evolution Reaction Catalytic Activity. *Advanced Materials*. 2018;30(18):1706076.
30. Kwon H, Ji B, Bae D, Lee J-H, Park HJ, Kim DH, et al. Role of anionic vacancy for active hydrogen evolution in WTe₂. *Applied Surface Science*. 2020;515:145972.
31. Zhou Y, Pondick JV, Silva JL, Woods JM, Hynek DJ, Matthews G, et al. Unveiling the Interfacial Effects for Enhanced Hydrogen Evolution Reaction on MoS₂/WTe₂ Hybrid Structures. *Small*. 2019;15(19):1900078.
32. Lee C-H, Silva EC, Calderin L, Nguyen MAT, Hollander MJ, Bersch B, et al. Tungsten Ditelluride: a layered semimetal. *Scientific Reports*. 2015;5(1):10013.
33. Zhao Y, Liu H, Yan J, An W, Liu J, Zhang X, et al. Anisotropic magnetotransport and exotic longitudinal linear magnetoresistance in WTe₂ crystals. *Physical Review B*. 2015;92(4):041104.
34. Bi R, Feng Z, Li X, Zhao J, Fan J, Shi Y, et al. Quantum oscillations of thermopower in WTe₂ thin films. *Physical Review B*. 2019;100(23):235405.
35. Chen K, Chen Z, Wan X, Zheng Z, Xie F, Chen W, et al. A Simple Method for Synthesis of High-Quality Millimeter-Scale 1T' Transition-Metal Telluride and Near-Field Nanooptical Properties. *Advanced Materials*. 2017;29(38):1700704.
36. Naylor CH, Parkin WM, Gao Z, Kang H, Noyan M, Wexler RB, et al. Large-area synthesis of high-quality monolayer 1T'-WTe₂ flakes. *2D Materials*. 2017;4(2):021008.
37. Zhou J, Liu F, Lin J, Huang X, Xia J, Zhang B, et al. Large-Area and High-Quality 2D Transition Metal Telluride. *Advanced Materials*. 2017;29(3):1603471.
38. Li J, Cheng S, Liu Z, Zhang W, Chang H. Centimeter-Scale, Large-Area, Few-Layer 1T'-WTe₂ Films by Chemical Vapor Deposition and Its Long-Term Stability in Ambient Condition. *The Journal of Physical Chemistry C*. 2018;122(12):7005-12.

39. de Melo O, Sánchez M, Borroto A, de Melo C, García BJ, Pau JL, et al. WTe₂ Synthesis by Tellurization of W Precursors Using Isothermal Close Space Vapor Transport Annealing. *physica status solidi (a)*. 2018;215(23):1800425.
40. Zhou Y, Jang H, Woods JM, Xie Y, Kumaravadivel P, Pan GA, et al. Direct Synthesis of Large-Scale WTe₂ Thin Films with Low Thermal Conductivity. *Advanced Functional Materials*. 2017;27(8):1605928.
41. Kwak J, Jo Y, Song S, Kim JH, Kim S-Y, Lee J-U, et al. Single-Crystalline Nanobelts Composed of Transition Metal Ditellurides. *Advanced Materials*. 2018;30(30):1707260.
42. Duffy R, Foley P, Filippone B, Mirabelli G, O'Connell D, Sheehan B, et al. Structural and Electrical Investigation of MoS₂ Thin Films Formed by Thermal Assisted Conversion of Mo Metal. *ECS Journal of Solid State Science and Technology*. 2016;5(11):Q3016-Q20.
43. Giri A, Yang H, Jang W, Kwak J, Thiyagarajan K, Pal M, et al. Synthesis of Atomically Thin Transition Metal Ditelluride Films by Rapid Chemical Transformation in Solution Phase. *Chemistry of Materials*. 2018;30(7):2463-73.
44. Walsh LA, Yue R, Wang Q, Barton AT, Addou R, Smyth CM, et al. W Te 2 thin films grown by beam-interrupted molecular beam epitaxy. *2D Materials*. 2017;4(2):025044.
45. Pan X-C, Chen X, Liu H, Feng Y, Wei Z, Zhou Y, et al. Pressure-driven dome-shaped superconductivity and electronic structural evolution in tungsten ditelluride. *Nature Communications*. 2015;6(1):7805.
46. Gong J-X, Yang J, Ge M, Wang Y-J, Liang D-D, Luo L, et al. Non-Stoichiometry Effects on the Extreme Magnetoresistance in Weyl Semimetal WTe₂. *Chinese Physics Letters*. 2018;35(9):097101.
47. Lu W, Zhang Y, Zhu Z, Lai J, Zhao C, Liu X, et al. Thin tungsten telluride layer preparation by thermal annealing. *Nanotechnology*. 2016;27(41):414006.
48. Woods JM, Shen J, Kumaravadivel P, Pang Y, Xie Y, Pan GA, et al. Suppression of Magnetoresistance in Thin WTe₂ Flakes by Surface Oxidation. *ACS Applied Materials & Interfaces*. 2017;9(27):23175-80.
49. Lee C-S, Oh SJ, Heo H, Seo S-Y, Kim J, Kim YH, et al. Epitaxial van der Waals Contacts between Transition-Metal Dichalcogenide Monolayer Polymorphs. *Nano Letters*. 2019;19(3):1814-20.
50. Woods JM, Hynek D, Liu P, Li M, Cha JJ. Synthesis of WTe₂ Nanowires with Increased Electron Scattering. *ACS Nano*. 2019;13(6):6455-60.
51. Song S, Sim Y, Kim S-Y, Kim JH, Oh I, Na W, et al. Wafer-scale production of patterned transition metal ditelluride layers for two-dimensional metal–semiconductor contacts at the Schottky–Mott limit. *Nature Electronics*. 2020.
52. Zhu X, Li S, Li J, Ali RN, Naz H, Liu P, et al. Free-standing WTe₂QD-doped NiSe/C nanowires for highly reversible lithium storage. *Electrochimica Acta*. 2019;295:22-8.
53. Vermeulen PA, Momand J, Kooi BJ. Low temperature epitaxy of tungsten–telluride heterostructure films. *CrystEngComm*. 2019;21(22):3409-14.
54. Chen Y, Chen Y, Ning J, Chen L, Zhuang W, He L, et al. Observation of Shubnikov-de Haas Oscillations in Large-Scale Weyl Semimetal WTe₂ Films. *Chinese Physics Letters*. 2020;37(1):017104.
55. Sun Y, Fujisawa K, Terrones M, Schaak RE. Solution synthesis of few-layer WTe₂ and MoxW_{1-x}Te₂ nanostructures. *Journal of Materials Chemistry C*. 2017;5(43):11317-23.

56. Mc Manus JB, Cunningham G, McEvoy N, Cullen CP, Gity F, Schmidt M, et al. Growth of 1T' MoTe₂ by Thermally Assisted Conversion of Electrodeposited Tellurium Films. *ACS Applied Energy Materials*. 2019;2(1):521-30.
57. Zhou L, Xu K, Zubair A, Zhang X, Ouyang F, Palacios T, et al. Role of Molecular Sieves in the CVD Synthesis of Large-Area 2D MoTe₂. *Advanced Functional Materials*. 2017;27(3):1603491.
58. Mc Manus JB, Horvath DV, Browne MP, Cullen CP, Cunningham G, Hallam T, et al. Low-temperature synthesis and electrocatalytic application of large-area PtTe₂ thin films. <https://arxiv.org/abs/200403199>. 2020:2004.03199.
59. Cao Y, Sheremetyeva N, Liang L, Yuan H, Zhong T, Meunier V, et al. Anomalous vibrational modes in few layer WTe₂ revealed by polarized Raman scattering and first-principles calculations. *2D Materials*. 2017;4(3):035024.
60. Jiang YC, Gao J, Wang L. Raman fingerprint for semi-metal WTe₂ evolving from bulk to monolayer. *Scientific Reports*. 2016;6(1):19624.
61. Ma H, Chen P, Li B, Li J, Ai R, Zhang Z, et al. Thickness-Tunable Synthesis of Ultrathin Type-II Dirac Semimetal PtTe₂ Single Crystals and Their Thickness-Dependent Electronic Properties. *Nano Letters*. 2018;18(6):3523-9.
62. Ma X, Guo P, Yi C, Yu Q, Zhang A, Ji J, et al. Raman scattering in the transition-metal dichalcogenides of 1T' MoTe₂ and Td WTe₂. *Physical Review B*. 2016;94(21):214105.
63. Ye F, Lee J, Hu J, Mao Z, Wei J, Feng PX-L. Environmental Instability and Degradation of Single- and Few-Layer WTe₂ Nanosheets in Ambient Conditions. *Small*. 2016;12(42):5802-8.
64. Shawkat MS, Gil J, Han SS, Ko T-J, Wang M, Dev D, et al. Thickness-Independent Semiconducting-to-Metallic Conversion in Wafer-Scale Two-Dimensional PtSe₂ Layers by Plasma-Driven Chalcogen Defect Engineering. *ACS Applied Materials & Interfaces*. 2020;12(12):14341-51.
65. Her YC, Huang SL. Growth mechanism of Te nanotubes by a direct vapor phase process and their room-temperature CO and NO₂ sensing properties. *Nanotechnology*. 2013;24(21):215603.
66. Predel B. *Phase Equilibria, Crystallographic and Thermodynamic Data of Binary Alloys*: Springer.
67. Callanan JE, Hope GA, Weir RD, Westrum EF. Thermodynamic properties of tungsten ditelluride (WTe₂) I. The preparation and lowtemperature heat capacity at temperatures from 6 K to 326 K. *The Journal of Chemical Thermodynamics*. 1992;24(6):627-38.
68. Srivastava SK, Avasthi BN. Layer type tungsten dichalcogenide compounds: their preparation, structure, properties and uses. *Journal of Materials Science*. 1985;20(11):3801-15.
69. Jones L, Nellist PD. Identifying and Correcting Scan Noise and Drift in the Scanning Transmission Electron Microscope. *Microscopy and Microanalysis*. 2013;19(4):1050-60.
70. Wenner S, Jones L, Marioara CD, Holmestad R. Atomic-resolution chemical mapping of ordered precipitates in Al alloys using energy-dispersive X-ray spectroscopy. *Micron*. 2017;96:103-11.
71. Jones L, Yang H, Pennycook TJ, Marshall MSJ, Van Aert S, Browning ND, et al. Smart Align—a new tool for robust non-rigid registration of scanning microscope data. *Advanced Structural and Chemical Imaging*. 2015;1(1):8.
72. Jones L. Quantitative ADF STEM: acquisition, analysis and interpretation. *IOP Conference Series: Materials Science and Engineering*. 2016;109:012008.

73. Jha R, Onishi S, Higashinaka R, Matsuda TD, Ribeiro RA, Aoki Y. Anisotropy in the electronic transport properties of Weyl semimetal WTe₂ single crystals. *AIP Advances*. 2018;8(10):101332.
74. Richoux V, Diliberto S, Boulanger C, Lecuire JM. Pulsed electrodeposition of bismuth telluride films: Influence of pulse parameters over nucleation and morphology. *Electrochimica Acta*. 2007;52(9):3053-60.
75. McEvoy N, Peltekis N, Kumar S, Rezvani E, Nolan H, Keeley GP, et al. Synthesis and analysis of thin conducting pyrolytic carbon films. *Carbon*. 2012;50(3):1216-26.

Synthesis of WTe₂ thin films and highly-crystalline nanobelts from pre-deposited reactants

*John B. Mc Manus^{1,2}, Cansu Ilhan^{1,2}, Bastien Balsamo^{2,3}, Clive Downing^{1,2}, Conor P. Cullen^{1,2},
Tanja Stimpfel-Lidner⁴, Graeme Cunningham^{1,2}, Lisanne Peters^{1,2}, Lewys Jones^{2,5}, Daragh
Mullarkey⁵, Igor V. Shvets⁵, Georg S. Duesberg^{1,4}, Niall McEvoy^{1,2*}*

¹ School of Chemistry, Trinity College Dublin, Dublin 2, D02 PN40, Ireland

² AMBER Centre, CRANN Institute, Trinity College Dublin, Dublin 2, D02 PN40, Ireland

³ SIGMA Clermont, Université Clermont Auvergne, F-63000 Clermont–Ferrand, France

⁴ Institute of Physics, EIT 2, Faculty of Electrical Engineering and Information Technology,
Universität der Bundeswehr, 85579 Neubiberg, Germany

⁵ School of Physics, Trinity College Dublin, Dublin 2, D02 PN40, Ireland

KEYWORDS: 2D materials; WTe₂; film conversion; electrodeposition; electron microscopy;
nanoelectronics

*Corresponding author: nmcevoy@tcd.ie

Supporting Information

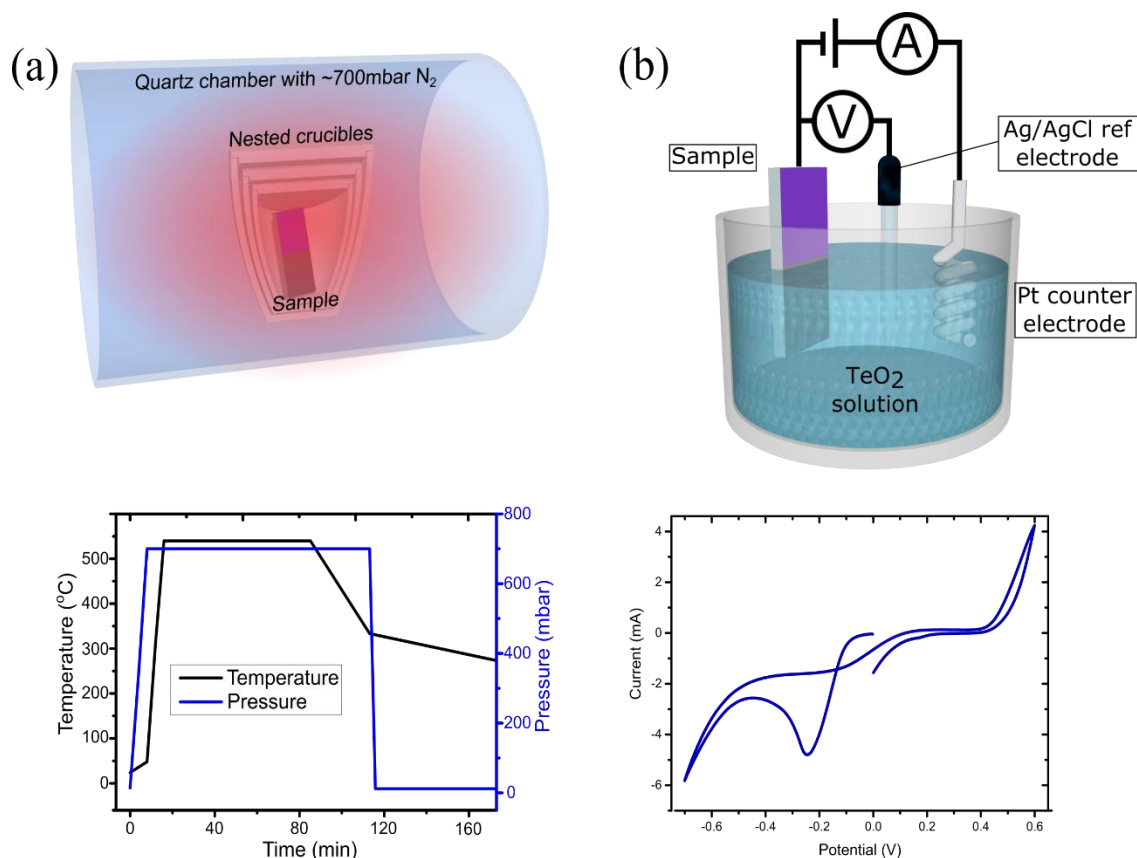


Fig S1: (a) Diagram of the quartz furnace and nested crucibles used to synthesize the WTe₂ films and nanobelts. Illustrative plot of typical temperature and pressure conditions in the furnace during the growth of the WTe₂. (b) Schematic of the Te electrodeposition process with the sample as the working electrode. Cyclic voltammogram of the cell showing the reduction peak at ~ -0.2 V corresponding to the electrodeposition of Te on the sample.

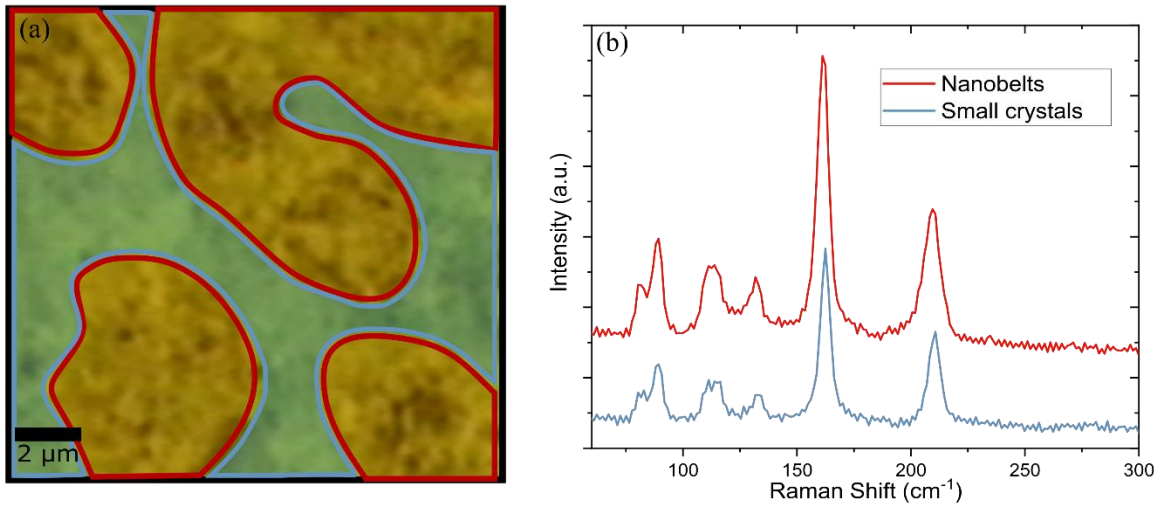


Fig. S2 (a) Optical image of a WTe_2 film. The areas enclosed in red are the patches of nanobelts. The areas highlighted blue are the smaller crystals that surround the patches of nanobelts. (b) Average Raman spectra corresponding to the two different morphology areas shown in (a). The red trace is the average Raman spectrum of the patches of nanobelts – red area in (a). The blue spectrum corresponds to the areas of smaller crystals. The expected WTe_2 modes in both indicates the presence of WTe_2 in both areas. The blue spectrum is less intense and slightly noisier, likely due to the smaller crystallite size in this area.

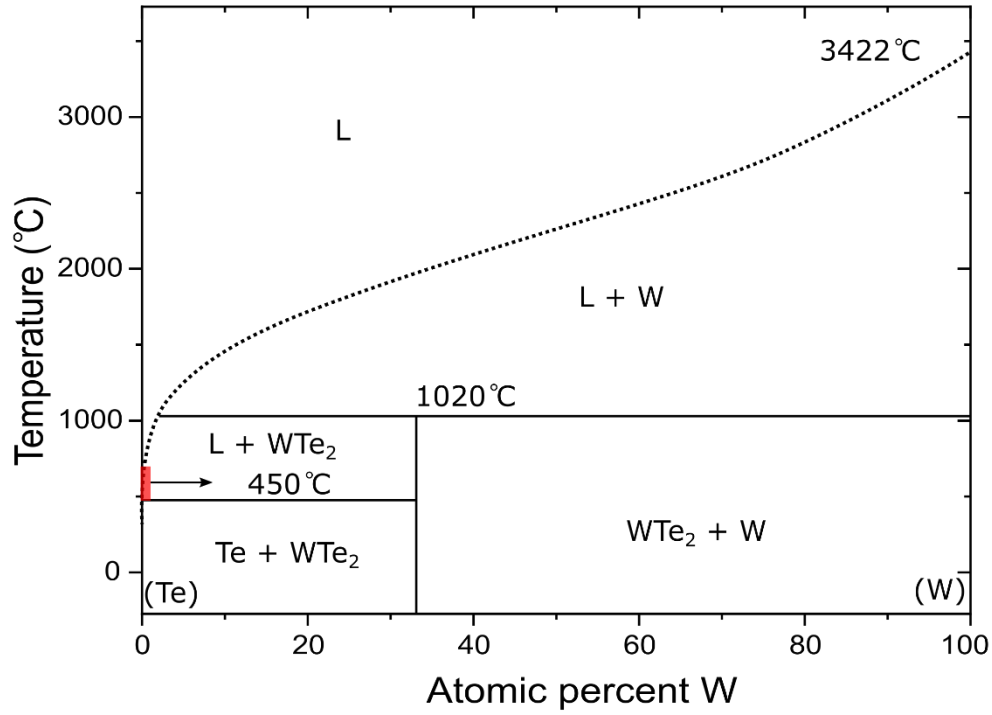


Fig. S3 Binary phase diagram for W-Te with temperature shown in degree Celcius, reproduced from reference.¹ The red area indicates the initial growth conditions for the WTe₂ in the liquid WTe_x alloy. The arrow indicates the direction that the overall system moves as the WTe₂ forms and the remaining Te evaporates.

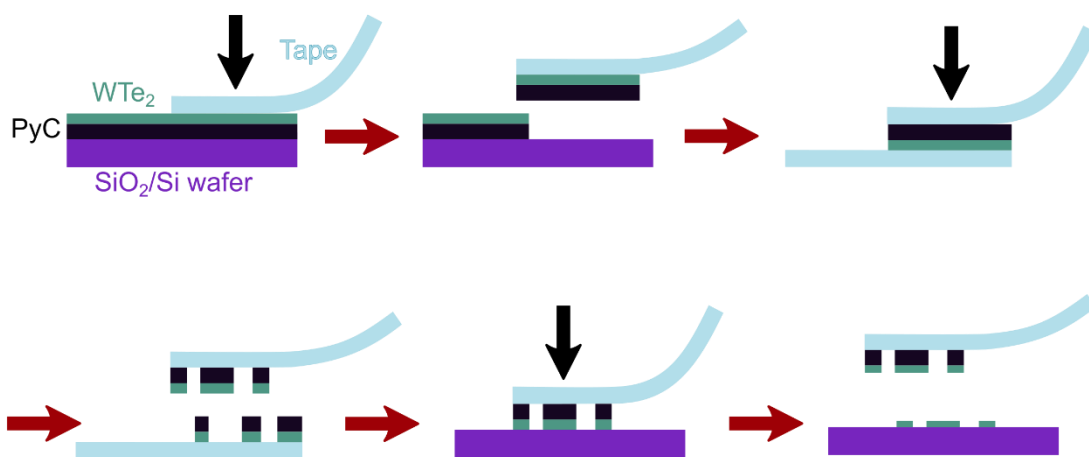


Figure S4: All samples were grown on PyC to aid the Te electrodeposition, however this did complicate the transfer somewhat. Firstly, a piece of tape was pressed down onto the sample with appropriate force (firm pressure under finger), before being removed, taking the WTe₂ and PyC layers with it. A second piece of tape was then pressed onto the first and removed. This second piece then had PyC in contact with the tape, and some WTe₂ nanobelts on top of this. This piece was then pressed onto a fresh SiO₂/Si wafer substrate and removed, resulting in WTe₂ nanobelts being deposited. This piece of tape could be used to deposit on multiple substrates, with each repetition giving less dense arrays of WTe₂ nanobelt. This technique was successfully used to transfer nanobelts for further analysis by TEM and for electrical device fabrication.

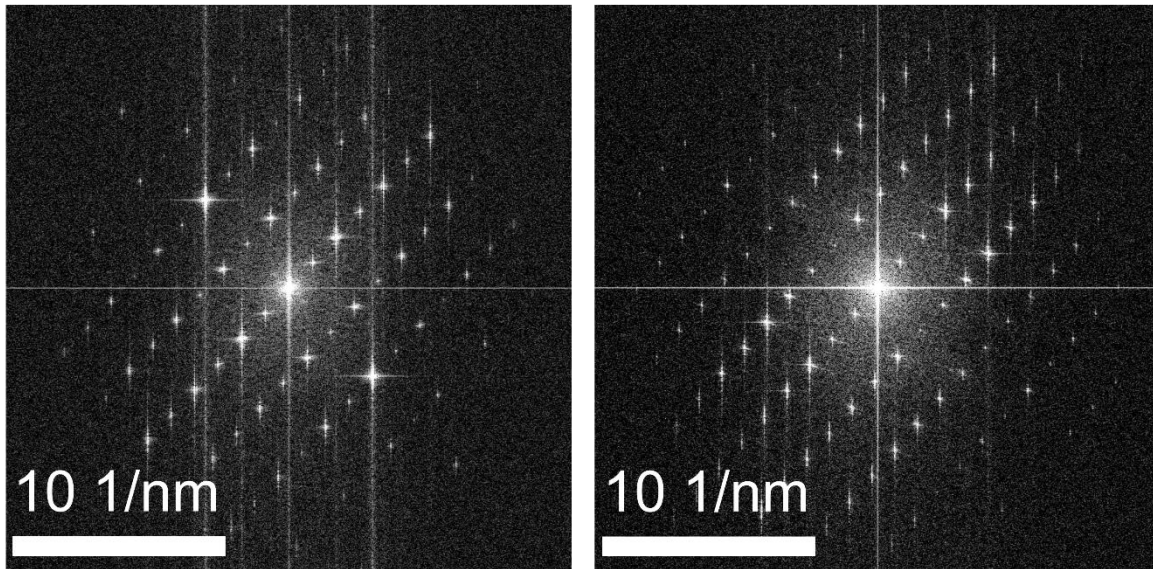


Fig. S5 FFT of images of opposite ends of a WTe_2 nanobelt. The similarity of these indicates that the same crystalline phase and orientation is present through the nanobelt.

References

1. Predel, B., *Phase Equilibria, Crystallographic and Thermodynamic Data of Binary Alloys*. Springer: Vol. 5.